







The Stars in M15 Were Born with the r -process*

Evan N. Kirby¹ , Gina Duggan¹ , Enrico Ramirez-Ruiz^{2,3} , and Phillip Macias² ¹ California Institute of Technology, 1200 East California Boulevard, MC 249-17, Pasadena, CA 91125, USA; enk@astro.caltech.edu² Department of Astronomy and Astrophysics, University of California, Santa Cruz, CA 95064, USA³ Niels Bohr Institute, University of Copenhagen, Blegdamsvej 17, DK-2100 Copenhagen, Denmark

Received 2019 December 2; revised 2020 February 13; accepted 2020 February 20; published 2020 March 2

Abstract

High-resolution spectroscopy of stars on the red giant branch (RGB) of the globular cluster M15 has revealed a large (~ 1 dex) dispersion in the abundances of r -process elements such as Ba and Eu. Neutron star mergers (NSMs) have been proposed as a major source of the r -process. However, most NSM models predict a delay time longer than the timescale for cluster formation. One possibility is that a NSM polluted the surfaces of stars in M15 long after the cluster finished forming. In this case, the abundances of the polluting elements would decrease in the first dredge-up as stars turn on to the RGB. We present Keck/DEIMOS abundances of Ba in 66 stars along the entire RGB and the top of the main sequence. The Ba abundances have no trend with stellar luminosity (evolutionary phase). Therefore, the stars were born with the Ba that they have today, and Ba did not originate in a source with a delay time longer than the timescale for cluster formation. In particular, if the source of Ba was a NSM, it would have had a very short delay time. Alternatively, if Ba enrichment took place before the formation of the cluster, an inhomogeneity of a factor of 30 in Ba abundance needs to be able to persist over the length scale of the gas cloud that formed M15, which is unlikely.

Unified Astronomy Thesaurus concepts: Globular star clusters (656); R -process (1324); Nucleosynthesis (1131)

1. Introduction

Elements beyond iron in the periodic table are made primarily via neutron capture, which can happen either slowly (s -process) or rapidly (r -process). While the s -process is known to occur primarily in asymptotic giant branch stars (Truran & Iben 1977; Karakas & Lattanzio 2014), there are still multiple candidate sites for the r -process (Lattimer & Schramm 1974; Qian & Wasserburg 2007). The gravitational wave-based discovery and subsequent electromagnetic observation of a kilonova in 2017 definitively showed that the r -process does occur in neutron star mergers (NSMs, e.g., Kasen et al. 2017). However, it is far from clear that NSMs are the sole site of the r -process (Hotokezaka et al. 2018; Côté et al. 2019).

The strongest argument that the r -process is also created in other events is that NSMs are expected to have long delay times ($\gtrsim 10^8$ yr, Kalogera et al. 2001). For example, it is difficult to explain the early appearance of the r -process in the Milky Way (MW) halo when it is assumed that metals are instantaneously mixed (van Oirschot et al. 2019). A more realistic treatment of mixing has resulted in differing conclusions on whether NSMs can explain the [Eu/Fe] scatter at low metallicities in the halo (Naiman et al. 2018; Haynes & Kobayashi 2019).

It is possible that the r -process source at late times (or high metallicity) is different from the source at early times (or low metallicity). At low metallicities in the MW halo (Macias & Ramirez-Ruiz 2018) and ultra-faint dwarf galaxies (Ji et al. 2016), the source seems to be rare and prolific, producing at least $10^{-3} M_{\odot}$ of r -process material per event. On the other hand, the r -process element Eu in the MW disk appears to be created in lockstep with Mg (e.g., Ishigaki et al. 2013), which is nearly

instantaneously recycled from core collapse supernovae (CCSNe). Therefore, it seems that the r -process source is not delayed at high metallicity or late times. Duggan et al. (2018) showed that the r -process component of Ba is delayed relative to CCSNe at $[\text{Fe}/\text{H}] < -1.6$ —but perhaps not at higher metallicities—in the Sculptor dwarf galaxy. However, Skúladóttir et al. (2019) argued that Eu in Sculptor shows no delay relative to Mg, although their data was limited in the metallicity range where Duggan et al. showed that r -process Ba is delayed.

There are two possibilities for synthesizing the r -process with a short delay. First, it is possible that there is a prompt population of NSMs. For example, the dynamics of dense star clusters can shorten the delay time compared to a NSM formed in the field (Ramirez-Ruiz et al. 2015). Second, there could be another major source of the r -process. Although the high-entropy wind surrounding the proto-neutron star of a CCSN was initially thought to be a promising site for r -process production (Meyer et al. 1992), most CCSN simulations fail to achieve the conditions required for the r -process (e.g., Qian & Woosley 1996). Alternatives include jet-driven, magnetorotational CCSNe (Nishimura et al. 2015) or the accretion disks around the supernovae that result from rapidly rotating massive stars (collapsars, Siegel et al. 2019). One issue with forming the r -process from massive stars is that observed stellar abundance distributions of metal-poor MW stars disfavor an r -process site that also produces iron (Macias & Ramirez-Ruiz 2019), which CCSNe are expected to produce. The current state of the field is that observations indicate that some r -process material comes from prompt sources, but it is difficult to produce the r -process in theoretical simulations of prompt sources.

Globular clusters (GCs) might be able to help show a fuller range of r -process production sites. GCs are complex sites of star formation. Almost all GCs show multiple chemical populations (Gratton et al. 2012), but no theory proposed so far can explain all of the nuances of the observed chemical abundance patterns (Bastian & Lardo 2018). The multiple

* The data presented herein were obtained at the W. M. Keck Observatory, which is operated as a scientific partnership among the California Institute of Technology, the University of California and the National Aeronautics and Space Administration. The Observatory was made possible by the generous financial support of the W. M. Keck Foundation.

populations in GCs are most evident in light elements, such as O and Na, but a small number of GCs possibly shows variations in neutron-capture elements (Roederer 2011). However, the evidence of a dispersion in some clusters has been called into question (Cohen 2011). The only incontrovertible example of this phenomenon is M15, which shows ~ 1 dex scatter in Ba, Eu, and other heavy elements (Sneden et al. 1997, 2000; Sobeck et al. 2011; Worley et al. 2013). The neutron-capture abundance pattern in nearly all GCs, including M15, is dominated by the r -process (e.g., Sneden et al. 2000).⁴ Therefore, some phenomenon must be able to pollute M15 inhomogeneously with the r -process. The inhomogeneity arises from a different source from the light elements because there is no correlation between the abundance variations in the light and neutron-capture elements in M15 or any other GC (Roederer 2011).

In this Letter, we investigate the possibility that the r -process in M15 was created by an NSM. Specifically, we consider an NSM with a “standard” delay time ($>10^8$ yr), much longer than the timescale of the formation of the cluster ($\sim 10^7$ yr). In this scenario, after the ejecta of the NSM sweeps up enough mass to cool (Montes et al. 2016), it would pollute already-formed stars via Bondi accretion. This scenario explains the star-to-star scatter in neutron-capture abundances because stars nearest to the NSM would have received the highest degree of pollution (see Tsujimoto & Shigejima 2014). The amount of r -process material in M15 is about the amount that a single NSM is expected to generate, which allows this scenario to be viable as long as most of the material is retained in the cluster. From the observed Eu abundances (Worley et al. 2013), we estimate that the stars in M15 contain about $8 \times 10^{-6} M_{\odot}$ of Eu, compared to $(3\text{--}15) \times 10^{-6} M_{\odot}$ generated by a single NSM (e.g., GW170817, Côté et al. 2018). The hypothesis predicts depletion of neutron-capture elements as stars ascend the red giant branch (RGB). We test this prediction with measurements of Ba abundances in M15 from the main sequence to the tip of the RGB.

2. Observations and Abundance Measurements

We observed a single slitmask with DEIMOS on the Keck II telescope on 2017 September 15. The slitmask, called 707811, was the same as that observed by Kirby et al. (2016). We used *BVRI* photometry from Stetson (1994). We chose targets from the RGB and main sequence turn-off (MSTO). The selection was performed by drawing a polygon around the locus of stars in the color–magnitude diagram (CMD). The width of the polygon was about 0.7 mag in $B - V$ color, which is wide enough to include effectively 100% of candidate member stars.

We used the 1200B diffraction grating at a central wavelength of 5500 Å. The approximate spectral range was 3900–4500 Å with a resolution of $\Delta\lambda = 1.1$ Å. We obtained 13 exposures of 20 minutes each for a total exposure time of 4.3 hr. The seeing was $0''.6$, and the transparency was good. We reduced the spectra with *spec2d* (Cooper et al. 2012; Newman et al. 2013), including our own modifications for the wavelength solution for the 1200B grating (see de los Reyes et al. 2020).

⁴ The major exception is Omega Centauri, which is either a GC or the nucleus of an accreted dwarf galaxy (Majewski et al. 2000). It has a large dispersion in [Ba/H], but the Ba seems to have been created in the s -process rather than the r -process (Smith et al. 2000).

Kirby et al. (2016) previously measured radial velocities, effective temperatures (T_{eff}), and metallicities ([Fe/H]) for the stars on this slitmask using DEIMOS’s 1200G diffraction grating. We used their membership determination, which enforced that members have radial velocities and metallicities within three standard deviations of their respective cluster means. We discarded the spectra of known non-members.

We measured Ba abundances using the procedure of Duggan et al. (2018). They constructed a grid of synthetic spectra over a range of T_{eff} , surface gravity ($\log g$), [Fe/H], and Ba abundance. The spectra were computed with MOOG (Sneden et al. 2012). The grid is searched for the Ba abundance that minimizes χ^2 between the grid and the observed spectrum. Some parameters (T_{eff} and $\log g$) were fixed at their previously determined values (Kirby et al. 2016). However, we enforced that [Fe/H] and $[\alpha/\text{Fe}]$ were the same for each star. In other words, we assumed that the intrinsic dispersion of these abundances in the cluster is essentially zero. The values were fixed at the median of the values determined by Kirby et al. (2016) for the stars in our present sample ([Fe/H] = -2.46 and $[\alpha/\text{Fe}] = 0.30$).⁵

The uncertainties on the Ba abundances are a combination of random uncertainty, which results from spectral noise, and systematic error, which results from a variety of sources, including imperfections in the spectral models. The systematic error of 0.1 dex was determined by Duggan et al. (2018). It is added in quadrature with the random uncertainty. As a result, 0.1 dex is the minimum error that we quote.

In some cases, we could not measure Ba abundances with uncertainties less than 0.5 dex. We treat these cases as upper limits. We quote the 90% C.L. upper limit by finding the Ba abundance that bounds 90% of the probability distribution. In some other cases, we were not even able to estimate an upper limit, due to excessive noise or anomalies in the spectra that affected the Ba lines. Table 1 gives the Ba abundances for all the M15 member stars in our sample. The table includes Ba measurements, upper limits, and non-measurements. The sample includes 96 stars, comprising 66 Ba abundance measurements, 15 upper limits, and 15 stars for which we were not able to measure Ba abundance or estimate an upper limit.

We used the local thermodynamic equilibrium (LTE) approximation in the spectral models and the atmospheres used to generate them. Some lines of Ba are subject to non-LTE corrections. Duggan et al. (2018) investigated the magnitude of the corrections (based on the work of Andrievsky et al. 2009) for 12 stars observed with DEIMOS over the ranges $3747 \text{ K} < T_{\text{eff}} < 5075 \text{ K}$ and $0.21 < \log g < 2.00$. The corrections to [Ba/Fe] ranged from -0.16 to $+0.15$. The more recent work of Eitner et al. (2019) found typical corrections of -0.2 for red giants. While these corrections would be important for some applications, we use our sample to look for changes in [Ba/Fe] greater than 1 dex (see Section 3). Therefore, our main conclusion is not affected by our approximation of LTE.

Figure 1 shows the DEIMOS spectra of four stars at different phases of evolution, from the main sequence to the tip of the RGB. The stars in the figure span a range

⁵ We also measured Ba abundances using [Fe/H] and $[\alpha/\text{Fe}]$ determined for each star. The mean Ba abundance decreased by 0.01 dex, and the standard deviation between the two methods was 0.08 dex. We conclude that both methods yield essentially identical results.

Table 1
Barium Abundances in M15

Star	R.A. (J2000)	Decl. (J2000)	$M_{V,0}$ (mag)	$(B - V)_0$ (mag)	v_{helio} (km s^{-1})	T_{eff} (K)	$\log g$ (cm s^{-2})	[Ba/H]
41376	21 29 59.34	+12 09 11.9	-2.87	1.26	-98.9 ± 2.1	4231	0.68	-2.42 ± 0.12
40809	21 29 59.17	+12 10 16.0	-2.56	1.15	-109.1 ± 2.1	4790	1.04	-2.14 ± 0.13
36569	21 29 57.94	+12 10 17.0	-2.44	1.02	-119.5 ± 2.1	4409	0.86	-1.95 ± 0.13
31227	21 29 56.32	+12 09 54.8	-2.24	1.06	-97.9 ± 2.1	4470	1.06	-2.18 ± 0.12
38742	21 29 58.55	+12 09 49.8	-2.13	1.21	-105.1 ± 2.1	5176	1.10	-2.98 ± 0.13
36913	21 29 58.04	+12 09 58.3	-1.85	0.77	-88.1 ± 2.1	4750	1.50	...
41670	21 29 59.43	+12 10 11.7	-1.85	0.91	-103.8 ± 2.1	4832	1.40	-2.19 ± 0.13
60808	21 30 15.67	+12 08 23.3	-1.62	0.90	-110.2 ± 2.1	4722	1.46	-2.32 ± 0.13
43593	21 30 00.05	+12 09 18.6	-1.49	0.80	-111.6 ± 2.1	4958	1.61	-1.76 ± 0.13
54055	21 30 06.97	+12 07 46.8	-1.48	0.72	-112.7 ± 2.1	5159	1.64	...
16135	21 29 43.55	+12 10 03.7	-1.33	0.79	-101.3 ± 2.1	4986	1.63	-1.69 ± 0.12
33889	21 29 57.17	+12 09 42.6	-1.20	0.86	-128.9 ± 2.1	4820	1.72	-2.25 ± 0.12
59959	21 30 14.28	+12 09 23.8	-1.12	0.82	-105.5 ± 2.1	4771	1.70	-2.16 ± 0.13
48120	21 30 01.83	+12 09 49.2	-1.06	0.75	-113.8 ± 2.1	4741	1.65	-2.13 ± 0.13
44027	21 30 00.19	+12 09 56.2	-1.02	0.80	-110.7 ± 2.1	4963	1.77	-2.47 ± 0.12
55914	21 30 08.96	+12 08 49.3	-1.00	0.79	-118.4 ± 2.1	4850	1.76	-2.16 ± 0.13
49483	21 30 02.77	+12 10 38.4	-0.97	0.66	-115.0 ± 2.1	5217	1.93	-1.74 ± 0.13
45688	21 30 00.76	+12 09 51.9	-0.96	0.79	-94.6 ± 2.1	4901	1.78	-2.26 ± 0.12
51057	21 30 04.02	+12 08 58.1	-0.87	0.79	-109.5 ± 2.1	4846	1.85	-2.42 ± 0.14
47982	21 30 01.75	+12 10 18.7	-0.83	0.79	-113.8 ± 2.1	4957	1.89	-1.99 ± 0.13
49428	21 30 02.74	+12 09 00.5	-0.80	0.73	-114.7 ± 2.1	4716	1.84	-2.41 ± 0.15
32206	21 29 56.66	+12 09 52.0	-0.63	0.59	-97.5 ± 2.1	5541	2.08	-2.54 ± 0.12
54512	21 30 07.50	+12 10 11.8	-0.56	0.72	-111.7 ± 2.1	4964	2.06	-2.61 ± 0.13
34335	21 29 57.30	+12 10 19.4	-0.53	0.69	-121.2 ± 2.1	4999	2.00	-2.29 ± 0.13
46494	21 30 01.06	+12 09 51.3	-0.47	0.78	-114.8 ± 2.1	4938	1.98	-2.62 ± 0.12
29005	21 29 55.28	+12 09 43.9	-0.45	0.73	-103.3 ± 2.1	4871	2.00	-2.42 ± 0.12
42594	21 29 59.73	+12 10 10.1	-0.43	0.74	-105.5 ± 2.1	5020	2.00	-2.29 ± 0.14
50124	21 30 03.27	+12 10 11.1	-0.37	0.74	-113.1 ± 2.1	4982	2.10	-1.65 ± 0.13
57863	21 30 11.27	+12 10 15.0	-0.33	0.83	-100.4 ± 2.1	4842	2.13	-1.86 ± 0.13
52787	21 30 05.58	+12 07 05.5	-0.27	0.72	-112.3 ± 2.1	5088	2.11	-2.37 ± 0.12
37854	21 29 58.30	+12 09 54.1	-0.27	0.62	-113.2 ± 2.1	4963	2.09	-2.25 ± 0.14
28721	21 29 55.13	+12 10 22.8	+0.11	0.27	-92.1 ± 2.2	6427	2.65	-2.86 ± 0.24
52771	21 30 05.57	+12 08 33.0	+0.47	0.69	-109.0 ± 2.1	5197	2.48	-1.74 ± 0.13
55135	21 30 08.16	+12 08 54.3	+0.66	0.62	-106.2 ± 2.1	5173	2.58	-2.11 ± 0.12
22822	21 29 50.80	+12 09 51.9	+0.81	0.61	-102.7 ± 2.1	5219	2.60	-2.38 ± 0.14
55541	21 30 08.54	+12 08 43.4	+1.22	0.55	-105.0 ± 2.1	5391	2.88	-1.92 ± 0.14
54237	21 30 07.18	+12 08 38.6	+1.33	0.59	-115.9 ± 2.1	5352	2.89	-2.04 ± 0.13
17122	21 29 44.89	+12 09 21.1	+1.39	0.58	-106.6 ± 2.1	5249	2.87	-2.71 ± 0.13
56979	21 30 10.17	+12 09 14.6	+1.42	0.60	-117.6 ± 2.1	5336	2.94	-2.36 ± 0.13
61191	21 30 16.32	+12 08 05.9	+1.44	0.58	-116.2 ± 2.1	5471	2.98	-2.01 ± 0.14
57312	21 30 10.57	+12 10 27.3	+1.49	0.63	-117.5 ± 2.1	5175	3.00	-1.97 ± 0.14
15681	21 29 42.91	+12 10 57.3	+1.63	0.60	-105.0 ± 2.1	5275	3.02	-1.99 ± 0.13
56947	21 30 10.14	+12 07 12.2	+1.82	0.59	-108.4 ± 2.2	5492	3.13	-2.30 ± 0.20
8920	21 29 28.21	+12 10 15.6	+1.93	0.57	-110.7 ± 2.2	5428	3.22	-2.60 ± 0.18
61776	21 30 17.39	+12 08 17.1	+2.08	0.59	-113.0 ± 2.5	5524	3.23	-2.35 ± 0.16
50825	21 30 03.82	+12 09 58.2	+2.15	0.65	-106.5 ± 2.2	5349	3.20	-2.21 ± 0.23
61068	21 30 16.10	+12 08 14.6	+2.17	0.48	-115.9 ± 2.2	5464	3.35	-1.68 ± 0.17
59374	21 30 13.38	+12 08 45.2	+2.19	0.61	-106.9 ± 2.2	5400	3.32	-2.07 ± 0.15
56251	21 30 09.34	+12 06 43.3	+2.19	0.56	-115.8 ± 2.2	5431	3.25	-2.75 ± 0.18
31125	21 29 56.28	+12 10 16.8	+2.20	0.67	-111.1 ± 2.1	4549	3.62	-1.56 ± 0.12
58363	21 30 11.91	+12 07 10.7	+2.20	0.51	-114.8 ± 2.2	5562	3.35	-2.25 ± 0.16
11998	21 29 36.32	+12 08 23.6	+2.32	0.56	-113.6 ± 2.2	5621	3.36	-2.71 ± 0.18
59071	21 30 12.95	+12 09 46.5	+2.34	0.54	-108.0 ± 2.3	5519	3.40	-1.64 ± 0.16
62219	21 30 18.20	+12 07 24.8	+2.41	0.49	-108.5 ± 2.3	5711	3.43	-2.11 ± 0.22
6374	21 29 17.88	+12 10 39.9	+2.77	0.50	-103.5 ± 4.9	6042	3.67	-2.33 ± 0.26
7175	21 29 21.57	+12 10 20.8	+2.80	0.50	-108.7 ± 2.4	5896	3.66	-2.08 ± 0.21
58890	21 30 12.65	+12 06 41.7	+2.84	0.46	-116.9 ± 2.4	5813	3.62	-2.95 ± 0.45
23303	21 29 51.28	+12 08 50.3	+3.00	0.44	-102.7 ± 2.3	6098	3.83	-2.36 ± 0.25
62661	21 30 19.09	+12 07 48.3	+3.12	0.34	-105.1 ± 2.9	6169	3.90	...
18956	21 29 47.04	+12 09 48.6	+3.14	0.35	-109.7 ± 2.7	6162	3.89	-2.51 ± 0.26
26974	21 29 54.04	+12 10 33.2	+3.16	0.51	-100.4 ± 2.9	6101	3.91	-1.81 ± 0.30
57247	21 30 10.48	+12 07 09.8	+3.17	0.42	-119.8 ± 3.1	6292	3.97	<-1.44
17384	21 29 45.18	+12 08 54.6	+3.18	0.40	-101.5 ± 2.5	6373	3.99	<-0.69

Table 1
(Continued)

Star	R.A. (J2000)	Decl. (J2000)	$M_{V,0}$ (mag)	$(B - V)_0$ (mag)	$v_{\text{helio}}^{(1)}$ (km s ⁻¹)	T_{eff} (K)	$\log g$ (cm s ⁻²)	[Ba/H]
28844	21 29 55.20	+12 10 53.9	+3.22	0.38	-108.6 ± 2.9	6439	4.06	<-0.42
18422	21 29 46.41	+12 09 46.4	+3.25	0.34	-103.7 ± 2.5	6213	3.93	-2.36 ± 0.30
22363	21 29 50.36	+12 10 30.8	+3.35	0.33	-104.6 ± 8.4	6263	4.01	-1.72 ± 0.46
12573	21 29 37.50	+12 08 13.7	+3.46	0.35	-115.3 ± 3.7	6258	4.13	...
18685	21 29 46.73	+12 10 38.1	+3.61	0.30	-109.6 ± 5.5	6173	4.07	-2.46 ± 0.37
16142	21 29 43.56	+12 08 47.3	+3.69	0.33	-106.8 ± 3.5	6557	4.29	<-1.66
27877	21 29 54.65	+12 10 58.7	+3.69	0.55	-100.5 ± 4.6	5875	4.05	<+0.30
16177	21 29 43.61	+12 09 17.1	+3.84	0.39	-119.4 ± 3.7	6093	4.17	-1.92 ± 0.36
8227	21 29 25.80	+12 11 45.7	+3.94	0.39	-113.3 ± 3.4	6709	4.38	-1.80 ± 0.37
12919	21 29 38.18	+12 10 32.8	+3.95	0.35	-100.3 ± 4.3	6536	4.28	<-1.07
12699	21 29 37.77	+12 09 02.4	+3.95	0.38	-108.3 ± 3.5	6791	4.38	-1.71 ± 0.38
22494	21 29 50.47	+12 08 59.0	+4.01	0.19	-99.3 ± 5.0	5962	4.20	...
7834	21 29 24.29	+12 12 10.4	+4.05	0.42	-115.3 ± 7.1	6575	4.34	...
7517	21 29 23.04	+12 10 54.4	+4.06	0.42	-109.1 ± 6.5	6705	4.40	<-1.16
8868	21 29 28.04	+12 11 46.2	+4.06	0.45	-104.7 ± 5.0	6663	4.43	...
10721	21 29 33.37	+12 08 04.5	+4.11	0.67	-97.9 ± 6.2	5010	3.97	<-2.04
25082	21 29 52.72	+12 07 52.8	+4.13	0.48	-114.6 ± 3.0	6560	4.37	<-1.36
8917	21 29 28.20	+12 08 17.2	+4.17	0.55	-105.4 ± 9.2	6368	4.42	<-1.30
9864	21 29 31.05	+12 09 01.0	+4.19	0.41	-113.2 ± 4.0	6323	4.36	<-1.48
7436	21 29 22.71	+12 09 00.6	+4.23	0.34	-119.0 ± 29.7	6541	4.41	-1.78 ± 0.46
8447	21 29 26.60	+12 11 46.1	+4.32	0.38	-114.5 ± 7.0	6496	4.41	-1.80 ± 0.45
24115	21 29 51.97	+12 10 13.2	+4.32	0.54	-97.4 ± 5.5	6113	4.36	<-1.01
7357	21 29 22.35	+12 10 59.0	+4.34	0.46	-106.5 ± 16.7	5825	4.30	...
10442	21 29 32.61	+12 08 47.1	+4.34	0.42	-104.6 ± 3.9	6495	4.50	...
18985	21 29 47.07	+12 10 16.2	+4.37	0.27	-110.7 ± 7.2	6120	4.35	...
14221	21 29 40.57	+12 09 52.3	+4.38	0.46	-104.9 ± 8.9	6490	4.44	<-1.18
25509	21 29 53.03	+12 09 59.7	+4.48	0.58	-100.4 ± 3.7	6186	4.49	...
11536	21 29 35.30	+12 08 17.2	+4.57	0.47	-86.5 ± 11.2	6155	4.44	<-0.08
24624	21 29 52.37	+12 08 39.7	+4.70	0.62	-86.5 ± 16.3	4750	1.50	...
15876	21 29 43.20	+12 10 25.4	+4.79	0.46	-100.6 ± 9.3	6249	4.50	<-0.85
8895	21 29 28.14	+12 11 18.0	+4.80	0.45	-117.2 ± 24.0	5537	4.40	...
14649	21 29 41.31	+12 09 35.4	+4.99	0.47	-104.2 ± 6.7	6193	4.57	...
11125	21 29 34.34	+12 10 44.6	+5.10	0.51	-88.0 ± 16.4	5145	4.34	...

Note. Photometry from Stetson (1994).

of 6.6 mag in the V -band. The corresponding range of spectral quality is apparent. The figure demonstrates how well the synthetic spectra fit the observed spectra. It also shows the response of the spectra to a change in Ba abundance of ± 0.3 dex. The individual Ba absorption lines in the fainter stars are at the edge of detectability. However, the spectral synthesis technique uses all of the information from five Ba lines (two of which are not shown in Figure 1) simultaneously. Thus, detections of individual lines are not a requirement for measuring abundances.

3. Mixing on the RGB

Low-mass stars, such as those in M15, experience mixing events as they evolve off the main sequence (see the review by Karakas & Lattanzio 2014). The first mixing episode is the first dredge-up (FDU), which occurs after the core is exhausted of hydrogen. The resulting contraction of the core drives the star to expand and its convective envelope to deepen. The FDU brings products of hydrogen burning (e.g., ^{13}C) to the surface. It also submerges and dilutes species that are only present on the stellar surface. The quintessential example of dilution at the FDU is ^7Li . Because ^7Li burns at a low temperature, it exists only in the outer layers of the star. The FDU dilutes the surface abundance as Li-poor material is dredged up to the surface.

The second mixing episode occurs at the luminosity function bump in the RGB. The convective envelope retreats in mass coordinate when the star is about halfway up the RGB. The retreating envelope leaves behind a discontinuity in mean molecular weight. As the hydrogen burning shell expands in mass coordinate, it eventually crosses this discontinuity, causing a brief pause in the star's ascent up the RGB. It is here that “extra mixing”—most likely thermohaline mixing (Charbonnel & Zahn 2007)—has been observed in several species, including C and Li (Gratton et al. 2000). The C and Li abundances drop because extra mixing connects the convective envelope to temperatures sufficient to burn ^{12}C and ^7Li through proton capture. This extra mixing is not expected to affect the abundance of Ba.

If an NSM polluted the surfaces of stars in M15 long after they formed, then the surface compositions of the stars would be different from their centers. Mixing at the FDU would dilute the r -process species that originated in the NSM. Therefore, we search for dilution signatures of Ba in M15 at the stellar luminosity that corresponds to the FDU.

To further quantify the observational signature of external pollution, we used Modules for Experimentation in Stellar Astrophysics (MESA; Paxton et al. 2011) to simulate the dilution at the FDU of an r -process pollution event. We simulated the post-main-sequence evolution of a $0.8 M_{\odot}$ star

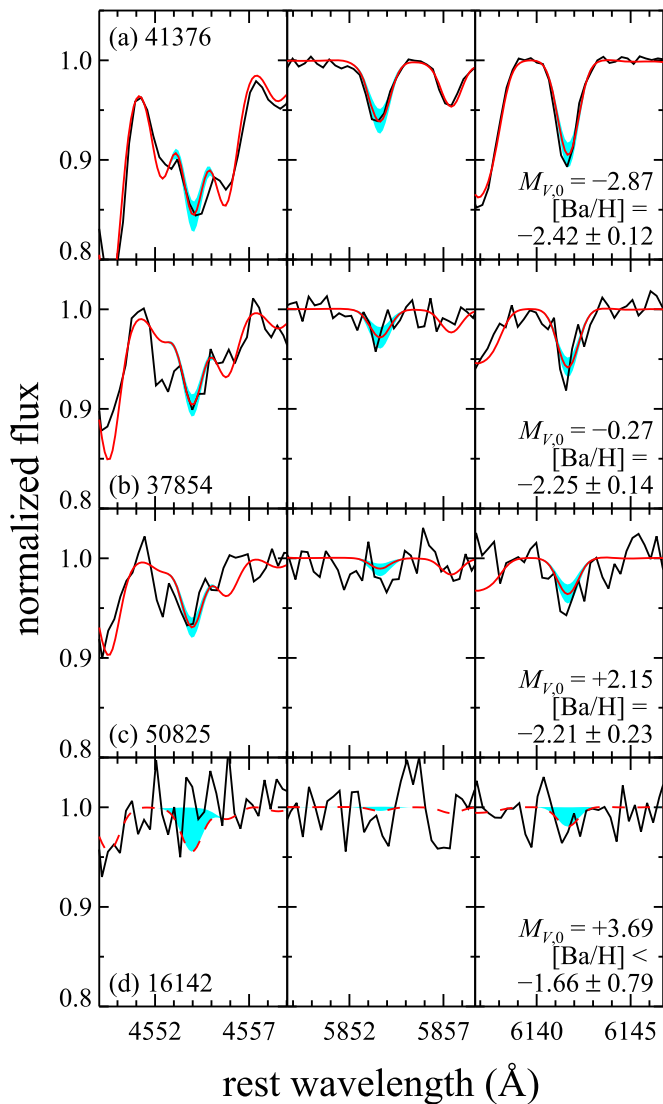


Figure 1. DEIMOS spectra for stars at various evolutionary stages: (a) tip of the RGB, (b) near the red clump, (c) near the end of the first dredge-up (FDU), and (d) just below the MSTO. Each panel lists the object name, extinction-corrected absolute V magnitude, and measured Ba abundance. Only small regions around three Ba lines are shown. The full spectral range is much larger, and the analysis uses two other Ba lines not shown here. The best-fitting synthetic spectra are shown in red, and the cyan regions show the response to a change in $[\text{Ba}/\text{H}]$ of ± 0.3 dex. The bottom panel shows an example of a 90% C.L. upper limit on Ba abundance, where the cyan region shows the response of the spectrum from changing the Ba abundance from the upper limit to zero.

with $[\text{Fe}/\text{H}] = -2$, roughly corresponding to stars at the MSTO in M15. In the simulation, some r -process material polluted the surface of the star when it was on the main sequence. Convection mixed this material throughout the convective envelope but no deeper. When the star turned off the main sequence, the FDU depleted the surface abundance of ^{153}Eu by a factor of ~ 30 , or 1.5 dex. If this scenario is occurring in M15, then we expect to see such a depletion in the abundances of all r -process elements, including our Ba measurements.

4. Results

Figure 2 summarizes our abundance measurements. The central panel shows the positions of our spectroscopic targets in the CMD in terms of absolute magnitude, where we used a

distance modulus of $m - M = 15.40$ (Durrell & Harris 1993). The right panel shows Ba abundances as a function of absolute magnitude. Where available, Ba upper limits are shown, but stars without Ba measurements are not indicated. For reference, the left panel shows Li abundance measurements in both M15 (Kirby et al. 2016) and NGC 6397 (Lind et al. 2009), another metal-poor GC. We use NGC 6397 as a benchmark because its proximity permits exquisite spectroscopy even at the main sequence. The Li measurements in M15 are not of sufficient quality to fully illustrate the mixing episodes. The detections of Li trace the upper envelope of the true underlying Li abundance distribution.

The Ba abundances exhibit the ~ 1 dex scatter that was already known to exist in M15. However, they show no trend with stellar luminosity. Excluding upper limits, the mean $[\text{Ba}/\text{H}]$ abundance at luminosities fainter than that expected for the FDU is -1.91 ± 0.15 , where the mean is weighted by the inverse square of the uncertainties, and the error bar is the standard error of the mean. The mean abundance is -2.23 ± 0.02 for stars brighter than the RGB bump, and -2.13 ± 0.03 for stars between the two mixing episodes. The abundances do not show the expected ~ 1.5 dex decrease at the FDU. As expected in any scenario, they also do not show a decline at the RGB bump.

The fact that the mean abundance is higher for main sequence stars is almost certainly a result of selection bias. The Ba measurements become less certain at fainter magnitudes, as reflected by the increasing error bars as a function of increasing magnitude in Figure 2. Furthermore, about half of the Ba abundances below the FDU are upper limits. Therefore, the mean abundance quoted above should also be viewed as an upper limit. We conclude that bias against Ba-poor faint stars causes at least some of the apparent dependence of Ba abundance on luminosity. Regardless, any observed decrease in abundance at the FDU is short of what we expected in the external pollution scenario.

5. Discussion

The giants would have lower Ba abundances than main sequence stars in M15 if Ba and other r -process elements originated in an NSM that occurred long after the cluster finished forming. We did not observe the expected decline in abundance. Therefore, Ba in M15 stars is well-mixed throughout the star. We conclude that the r -process elements in M15 were generated before or during the formation of the cluster. If the enrichment happened before the formation of the cluster, an inhomogeneity of a factor of 30 in r -process abundance needs to persist over the length scale of the protogiant molecular cloud that formed M15. However, such large abundance fluctuations might be difficult to preserve at parsec scales (Montes et al. 2016).

This is not the first study to measure the abundances of neutron-capture elements on the main sequence in GCs. Other clusters with measurements of neutron-capture abundances on or near the main sequence include M92 (King et al. 1998), M5 (Ramírez & Cohen 2003), 47 Tuc, NGC 6397, NGC 6752 (James et al. 2004a, 2004b), and M13 (Cohen & Meléndez 2005). In no cluster does the abundance of heavy elements depend on evolutionary state. The unique aspect of this study is that M15 was an especially interesting candidate due to its large scatter in neutron-capture abundances, which might be expected if the NSM had preferentially polluted the stars closest to it.

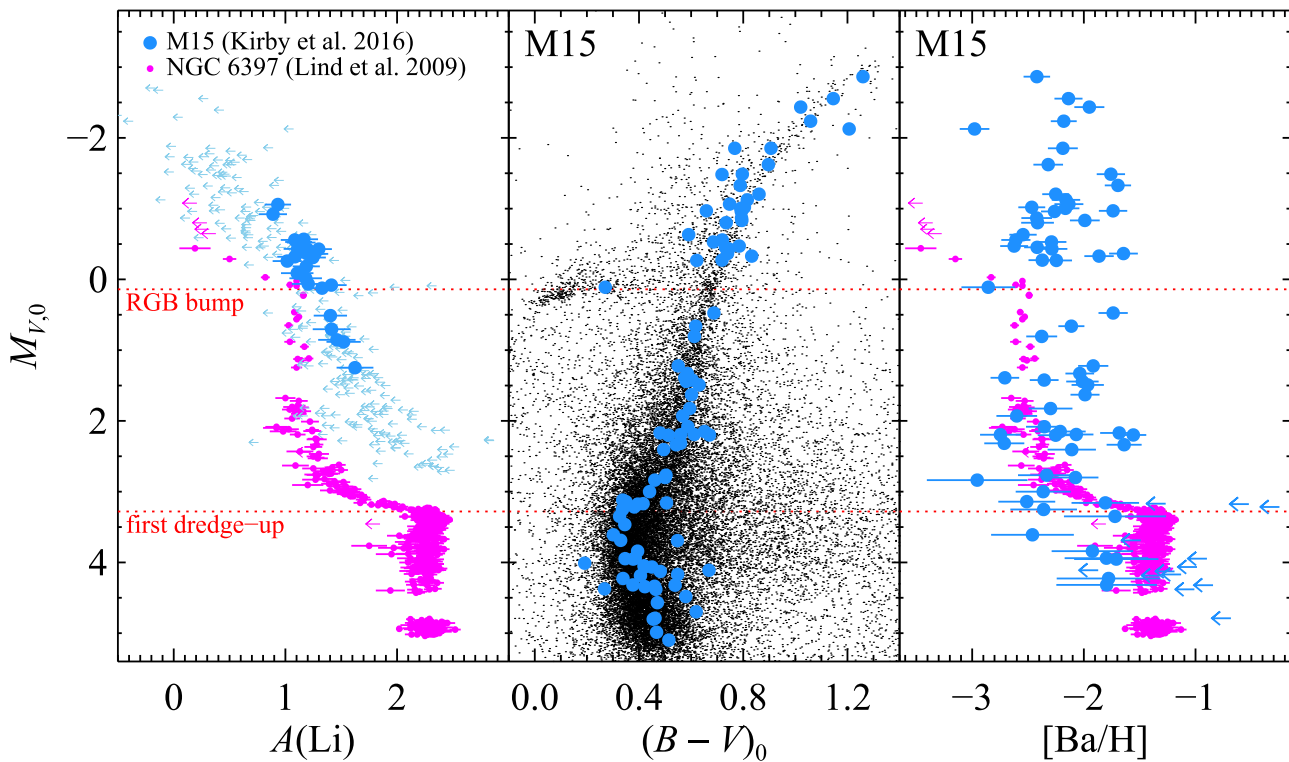


Figure 2. Left: as stars evolve up the RGB, Li is diluted. Measurements in M15 from DEIMOS (Kirby et al. 2016) are shown as large blue points and light blue upper limits. Higher-quality measurements in NGC 6397 (small magenta points and upper limits; Lind et al. 2009) are also shown as a clearer demonstration of the dilution. Center: the CMD of M15 (small points, Stetson 1994). Stars with Ba abundance measurements from DEIMOS are shown as large blue points. Right: DEIMOS measurements of $[\text{Ba}/\text{H}]$ for stars at a variety of evolutionary phases in M15 (blue) including some upper limits (large, leftward-pointing blue arrows). The Li abundances in NGC 6397, shifted by an arbitrary constant, are shown in magenta to illustrate the expected dilution if Ba were present only on the stellar surface. The blue points in the center and right panels represent the same stars. Red dotted lines indicate the absolute magnitudes of the FDU and RGB bump.

Our study rules out a source with a delay time greater than the cluster formation time, but it does not necessarily rule out an NSM altogether. As mentioned earlier, dense cluster environments can accelerate the dynamical evolution of compact binaries so that the NSM delay times would be shorter than in the field (Ramirez-Ruiz et al. 2015). However, M15 is likely not dense enough to cause dynamically driven NSMs. Still, Zevin et al. (2019) argued that it is possible for a binary neutron star system, formed from the first generation of stars in the GC, to merge within the cluster’s star formation timescale (30–50 Myr). This scenario requires many conditions to be true, including Case BB mass transfer (i.e., after the end of He core burning) and the ability for the NSM to enrich the cluster despite any natal kick. Alternatively, Bekki & Tsujimoto (2017) proposed that the formation of M15 might have had a duration of ~ 0.1 Gyr, long enough for an NSM to enrich the stars forming in the cluster. In support of this scenario, Beniamini & Piran (2019) found that about 40% observed binary neutron stars in the MW have short (< 1 Gyr) merging times. These include two systems discovered decades ago with merging times of 0.3–0.4 Gyr (e.g., Phinney 1991) and three others discovered more recently with merging times less than 0.1 Gyr (e.g., Stovall et al. 2018).

In summary, we have ruled out one scenario for r -process enrichment in M15, but the possibilities remain numerous.

We are grateful to Marc Kassis, Carlos Álvarez, and Percy Gómez for their essential roles in providing DEIMOS with the 1200B diffraction grating. We thank Paz Beniamini, E. Sterl Phinney, and Shrinivas Kulkarni for directing us to

the observational studies of merging times for binary neutron stars. We also thank Dan Kasen and Ryan Foley for helpful discussions, and the anonymous referee for a helpful report.

This material is based upon work supported by the National Science Foundation under grant No. AST-1847909. E.N.K. gratefully acknowledges support from a Cottrell Scholar award administered by the Research Corporation for Science Advancement as well as funding from generous donors to the California Institute of Technology. E.R.-R. and P.M. thank the Heising-Simons Foundation, the Danish National Research Foundation (DNRF132), and NSF (AST-1911206 and AST-1852393) for support.

We are grateful to the many people who have worked to make the Keck Telescope and its instruments a reality and to operate and maintain the Keck Observatory. The authors wish to extend special thanks to those of Hawaiian ancestry on whose sacred mountain we are privileged to be guests. Without their generous hospitality, none of the observations presented herein would have been possible.

Facility: Keck:II (DEIMOS).

Software: spec2d (Cooper et al. 2012; Newman et al. 2013), MOOG (Snedden et al. 2012), MESA (Paxton et al. 2011).

ORCID iDs

Evan N. Kirby <https://orcid.org/0000-0001-6196-5162>

Gina Duggan <https://orcid.org/0000-0002-9256-6735>

Enrico Ramirez-Ruiz <https://orcid.org/0000-0003-2558-3102>

Phillip Macias <https://orcid.org/0000-0002-9946-4635>

References

- Andrievsky, S. M., Spite, M., Korotin, S. A., et al. 2009, *A&A*, **494**, 1083
- Bastian, N., & Lardo, C. 2018, *ARA&A*, **56**, 83
- Bekki, K., & Tsujimoto, T. 2017, *ApJ*, **844**, 34
- Beniamini, P., & Piran, T. 2019, *MNRAS*, **487**, 4847
- Charbonnel, C., & Zahn, J.-P. 2007, *A&A*, **467**, L15
- Cohen, J. G. 2011, *ApJL*, **740**, L38
- Cohen, J. G., & Meléndez, J. 2005, *AJ*, **129**, 303
- Cooper, M. C., Newman, J. A., Davis, M., Finkbeiner, D. P., & Gerke, B. F. 2012, spec2d: DEEP2 DEIMOS Spectral Pipeline, Astrophysics Source Code Library, ascl:1203.003
- Côté, B., Eichler, M., Arcones, A., et al. 2019, *ApJ*, **875**, 106
- Côté, B., Fryer, C. L., Belczynski, K., et al. 2018, *ApJ*, **855**, 99
- de los Reyes, M. A. C., Kirby, E. N., & Shen, K. J. 2020, *ApJ*, in press (arXiv:2001.01716)
- Duggan, G. E., Kirby, E. N., Andrievsky, S. M., & Korotin, S. A. 2018, *ApJ*, **869**, 50
- Durrell, P. R., & Harris, W. E. 1993, *AJ*, **105**, 1420
- Eitner, P., Bergemann, M., & Larsen, S. 2019, *A&A*, **627**, A40
- Gratton, R. G., Carretta, E., & Bragaglia, A. 2012, *A&ARv*, **20**, 50
- Gratton, R. G., Sneden, C., Carretta, E., & Bragaglia, A. 2000, *A&A*, **354**, 169
- Haynes, C. J., & Kobayashi, C. 2019, *MNRAS*, **483**, 5123
- Hotokezaka, K., Beniamini, P., & Piran, T. 2018, *IJMPD*, **27**, 1842005
- Ishigaki, M. N., Aoki, W., & Chiba, M. 2013, *ApJ*, **771**, 67
- James, G., François, P., Bonifacio, P., et al. 2004a, *A&A*, **427**, 825
- James, G., François, P., Bonifacio, P., et al. 2004b, *A&A*, **414**, 1071
- Ji, A. P., Frebel, A., Chiti, A., & Simon, J. D. 2016, *Natur*, **531**, 610
- Kalogera, V., Narayan, R., Spergel, D. N., & Taylor, J. H. 2001, *ApJ*, **556**, 340
- Karakas, A. I., & Lattanzio, J. C. 2014, *PASA*, **31**, e030
- Kasen, D., Metzger, B., Barnes, J., Quataert, E., & Ramirez-Ruiz, E. 2017, *Natur*, **551**, 80
- King, J. R., Stephens, A., Boesgaard, A. M., & Deliyannis, C. 1998, *AJ*, **115**, 666
- Kirby, E. N., Guhathakurta, P., Zhang, A. J., et al. 2016, *ApJ*, **819**, 135
- Lattimer, J. M., & Schramm, D. N. 1974, *ApJL*, **192**, L145
- Lind, K., Primas, F., Charbonnel, C., Grundahl, F., & Asplund, M. 2009, *A&A*, **503**, 545
- Macias, P., & Ramirez-Ruiz, E. 2018, *ApJ*, **860**, 89
- Macias, P., & Ramirez-Ruiz, E. 2019, *ApJL*, **877**, L24
- Majewski, S. R., Patterson, R. J., Dinescu, D. I., et al. 2000, in Liege Int. Astrophys. Coll. 35, The Galactic Halo: From Globular Cluster to Field Stars, ed. A. Noels et al. (Liege: Institut d'Astrophysique et de Geophysique), 619
- Meyer, B. S., Mathews, G. J., Howard, W. M., Woosley, S. E., & Hoffman, R. D. 1992, *ApJ*, **399**, 656
- Montes, G., Ramirez-Ruiz, E., Naiman, J., Shen, S., & Lee, W. H. 2016, *ApJ*, **830**, 12
- Naiman, J. P., Pillepich, A., Springel, V., et al. 2018, *MNRAS*, **477**, 1206
- Newman, J. A., Cooper, M. C., Davis, M., et al. 2013, *ApJS*, **208**, 5
- Nishimura, N., Takiwaki, T., & Thielemann, F.-K. 2015, *ApJ*, **810**, 109
- Paxton, B., Bildsten, L., Dotter, A., et al. 2011, *ApJS*, **192**, 3
- Phinney, E. S. 1991, *ApJL*, **380**, L17
- Qian, Y. Z., & Wasserburg, G. J. 2007, *PhR*, **442**, 237
- Qian, Y. Z., & Woosley, S. E. 1996, *ApJ*, **471**, 331
- Ramírez, S. V., & Cohen, J. G. 2003, *AJ*, **125**, 224
- Ramirez-Ruiz, E., Trenti, M., MacLeod, M., et al. 2015, *ApJL*, **802**, L22
- Roederer, I. U. 2011, *ApJL*, **732**, L17
- Siegel, D. M., Barnes, J., & Metzger, B. D. 2019, *Natur*, **569**, 241
- Skúladóttir, Á., Hansen, C. J., Salvadori, S., & Choplin, A. 2019, *A&A*, **631**, A171
- Smith, V. V., Suntzeff, N. B., Cunha, K., et al. 2000, *AJ*, **119**, 1239
- Sneden, C., Bean, J., Ivans, I., Lucatello, S., & Sobeck, J. 2012, LTE Line Analysis and Spectrum Synthesis, Version 2017, Astrophysics Source Code Library, ascl:1202.009
- Sneden, C., Johnson, J., Kraft, R. P., et al. 2000, *ApJL*, **536**, L85
- Sneden, C., Kraft, R. P., Shetrone, M. D., et al. 1997, *AJ*, **114**, 1964
- Sobeck, J. S., Kraft, R. P., Sneden, C., et al. 2011, *AJ*, **141**, 175
- Stetson, P. B. 1994, *PASP*, **106**, 250
- Stovall, K., Freire, P. C. C., Chatterjee, S., et al. 2018, *ApJL*, **854**, L22
- Truran, J. W., & Iben, I. J. 1977, *ApJ*, **216**, 797
- Tsujimoto, T., & Shigeeyama, T. 2014, *ApJL*, **795**, L18
- van Oirschot, P., Nelemans, G., Pols, O., & Starkeburg, E. 2019, *MNRAS*, **483**, 4397
- Worley, C. C., Hill, V., Sobeck, J., & Carretta, E. 2013, *A&A*, **553**, A47
- Zevin, M., Kremer, K., Siegel, D. M., et al. 2019, *ApJ*, **886**, 4